TRANSONIC FLOW OVER A DELTA WING USING A $k-\epsilon$ TURBULENCE MODEL

ICAS-94-2.3.2

Timo Siikonen, Petri Kaurinkoski and Seppo Laine

Laboratory of Aerodynamics
Helsinki University of Technology
FIN-02150 Espoo, Finland

Abstract

Transonic viscous flow around a cropped delta wing with a round leading edge is investigated by solving the Reynolds averaged thin-layer Navier–Stokes equations. A low Reynolds number $k-\epsilon$ turbulence model is used for the evaluation of the turbulent viscosities. The angle of attack is either 10 or 20 degrees, the Mach number is 0.85 and the Reynolds number based on the root chord is 4.5×10^6. The results are compared with experiments.

Introduction

Despite the increase in computing power, there are several aspects in the solution of the Navier–Stokes equations that remain unsolved. A major problem is the accuracy of the turbulence modelling. Several algebraic turbulence models[1,2] exist for attached flows, but those models can treat neither complex geometries nor separated flows properly. Another major drawback of the algebraic models is the inability to take account of history effects.

Recently, the trend has been to implement more sophisticated two-equation turbulence models to Navier–Stokes codes. More sophisticated and complex models require more computing power, but since they have more physics behind them, they are expected to produce more accurate results. These models, such as the $k-\epsilon$ model[3] are usually not very suitable for high-Reynolds number flows with thin boundary layers. The presence of a solid wall has to be modelled separately. The original approach with the $k-\epsilon$ model is to use wall functions, which requires a complicated boundary treatment. Another approach, applied in the present work, is to use low-Reynolds number models, in which the presence of a solid wall is taken into account in the source terms and in the calculation of turbulent viscosity.

In the present study the flow past a cropped delta wing at transonic speed is solved using Chien's low-Reynolds number $k-\epsilon$ turbulence model[4]. The investigated wing is the round leading edge delta wing with a leading edge sweep angle of 65° examined in the International Vortex Flow Experiment on Euler Code Validation[5]. Previously, the same wing has been calculated using both Euler and Navier–Stokes codes.

The Reynolds number of the calculated cases is 4.5×10^6, and therefore the calculations are performed with a totally turbulent boundary layer. Previously, these cases have been calculated using the Cebeci–Smith turbulence model [6]. In the present study, emphasis is laid on differences between the solutions obtained using the Cebeci–Smith model and the $k-\epsilon$ model. The angle of attack is either 10.76° or 19.48°, but detailed results are presented only for the case $\alpha = 10.76°$.

The calculations are performed with a Navier–Stokes code called FINFLO that solves the Reynolds averaged thin-layer Navier–Stokes equations by a finite-volume method. The scheme applies the flux-difference splitting of Roe [7] and the time integration method is implicit. A multigrid V-cycle is used to accelerate the convergence. The code has been developed at the Laboratory of Aerodynamics in the Helsinki University of Technology and is described in Refs.[8,9] .

Numerical Method

Governing Equations

The Reynolds averaged Navier–Stokes equations, and the equations for the the kinetic energy k and dissipation ϵ of turbulence can be written in the following form

$$\frac{\partial U}{\partial t}+\frac{\partial (F-F_v)}{\partial x}+\frac{\partial (G-G_v)}{\partial y}+\frac{\partial (H-H_v)}{\partial z}=Q \quad (1)$$

where $U=(\rho,\ \rho u,\ \rho v,\ \rho w,\ E,\ \rho k,\ \rho\epsilon)^T$. The inviscid fluxes are

$$F=\begin{pmatrix} \rho u \\ \rho u^2+p+\frac{2}{3}\rho k \\ \rho vu \\ \rho wu \\ (E+p+\frac{2}{3}\rho k)u \\ \rho uk \\ \rho u\epsilon \end{pmatrix} \qquad G=\begin{pmatrix} \rho v \\ \rho uv \\ \rho v^2+p+\frac{2}{3}\rho k \\ \rho wv \\ (E+p+\frac{2}{3}\rho k)v \\ \rho vk \\ \rho v\epsilon \end{pmatrix} \quad (2)$$

$$H = \begin{pmatrix} \rho w \\ \rho uw \\ \rho vw \\ \rho w^2 + p + \frac{2}{3}\rho k \\ (E + p + \frac{2}{3}\rho k)w \\ \rho wk \\ \rho w\epsilon \end{pmatrix}$$

Here ρ is the density; the velocity is $\vec{V} = u\vec{i} + v\vec{j} + w\vec{k}$; p is the pressure, and E the total internal energy defined as

$$E = \rho e + \frac{\rho \vec{V} \cdot \vec{V}}{2} + \rho k \tag{3}$$

where e is the internal energy. The pressure is calculated from the perfect gas law

$$p = (\gamma - 1)\rho e \tag{4}$$

where γ is the ratio of specific heats c_p/c_v. The source term Q has non-zero components, which will be given later, only for turbulence equations. The viscous fluxes are

$$F_v = \begin{pmatrix} 0 \\ \tau_{xx} \\ \tau_{xy} \\ \tau_{xz} \\ u\tau_{xx} + v\tau_{xy} + w\tau_{xz} - q_x \\ \mu_k(\partial k/\partial x) \\ \mu_\epsilon(\partial \epsilon/\partial x) \end{pmatrix}$$

$$G_v = \begin{pmatrix} 0 \\ \tau_{xy} \\ \tau_{yy} \\ \tau_{yz} \\ u\tau_{xy} + v\tau_{yy} + w\tau_{yz} - q_y \\ \mu_k(\partial k/\partial y) \\ \mu_\epsilon(\partial \epsilon/\partial y) \end{pmatrix} \tag{5}$$

$$H_v = \begin{pmatrix} 0 \\ \tau_{xz} \\ \tau_{yz} \\ \tau_{zz} \\ u\tau_{xz} + v\tau_{yz} + w\tau_{zz} - q_z \\ \mu_k(\partial k/\partial z) \\ \mu_\epsilon(\partial \epsilon/\partial z) \end{pmatrix}$$

For the Reynolds stresses, we apply Boussinesq's approximation

$$-\overline{\rho u_i'' u_j''} = \mu_T[\frac{\partial u_j}{\partial x_i} + \frac{\partial u_i}{\partial x_j} - \frac{2}{3}(\nabla \cdot \vec{V})\delta_{ij}] - \frac{2}{3}\rho k \delta_{ij} \tag{6}$$

where μ_T is a turbulent viscosity coefficient. The molecular viscosity is calculated from Sutherland's formula. In the $k - \epsilon$ model the turbulent viscosity is calculated from

$$\mu_T = c_\mu \frac{\rho k^2}{\epsilon} \frac{Re_\infty}{Ma_\infty} \tag{7}$$

In the momentum and energy equations the kinetic energy contribution has been connected with pressure and appears in the inviscid fluxes. The viscous terms contain a laminar and turbulent part. Similarly, the heat flux is written as

$$\vec{q} = -(k + k_T)\nabla T = -(\mu \frac{c_p}{Pr} + \mu_T \frac{c_p}{Pr_T})\nabla T \tag{8}$$

where k and k_T are molecular and turbulent thermal conductivity coefficients and Pr and Pr_T are laminar and turbulent Prandtl numbers, respectively. In this study $Pr = 0.72$ and $Pr_T = 0.9$ are used. The diffusion of turbulence variables is modelled as

$$\mu_k \nabla k = (\mu + \frac{\mu_T}{\sigma_k})\nabla k \tag{9}$$

$$\mu_\epsilon \nabla \epsilon = (\mu + \frac{\mu_T}{\sigma_\epsilon})\nabla \epsilon \tag{10}$$

where σ_k and σ_ϵ are empirical coefficients.

The equations are scaled with free-stream speed of sound c_∞, density ρ_∞, temperature T_∞, viscosity μ_∞ and reference length L_∞. In particular, the nondimensionalized kinetic energy and dissipation of turbulence are expressed as $k^* = k/c_\infty^2$ and $\epsilon^* = \epsilon/(c_\infty^3/L_\infty)$. The present scaling retains the form of the inviscid fluxes, whereas the stress terms have to be multiplied by Ma_∞/Re_∞. In the following, scaled variables are used and the superscripts have been dropped for simplicity.

Source Term

Near the wall the low-Reynolds number model proposed by Chien [4] is adopted. The source term for Chien's model is given as

$$Q = \begin{pmatrix} P - \rho\epsilon - 2\frac{Ma_\infty}{Re_\infty}\mu\frac{k}{y_n^2} \\ c_1\frac{\epsilon}{k}P - c_2\frac{\rho\epsilon^2}{k} - 2\frac{Ma_\infty}{Re_\infty}\mu\frac{\epsilon}{y_n^2}e^{-y^+/2} \end{pmatrix} \tag{11}$$

where y_n is the normal distance from the wall, and y^+ is defined by

$$y^+ = y_n\Big[\frac{Re_\infty}{Ma_\infty}\frac{\rho|\nabla \times \vec{V}|}{\mu}\Big]_w^{1/2} \tag{12}$$

The production of turbulent kinetic energy is modelled using Eq.(6)

$$\begin{aligned} P &= -\rho u_i'' u_j'' \frac{\partial u_i}{\partial x_j} \\ &= [\mu_T(\frac{\partial u_i}{\partial x_j} + \frac{\partial u_j}{\partial x_i} - \frac{2}{3}\delta_{ij}\frac{\partial u_k}{\partial x_k}) - \frac{2}{3}\delta_{ij}\rho k]\frac{\partial u_i}{\partial x_j} \end{aligned} \tag{13}$$

The source as well as the equations for k and ϵ contain empirical coefficients. In the present study, we have applied the following set of coefficients

$$\begin{aligned} c_1 &= 1.44 & c_2 &= 1.92(1 - 0.22e^{-Re_T^2/36}) \\ \sigma_k &= 1.0 & c_\mu &= 0.09(1 - e^{-0.0115y^+}) \\ \sigma_\epsilon &= 1.3 \end{aligned}$$

where the turbulence Reynolds number is defined as

$$Re_T = \frac{\rho k^2}{\mu\epsilon}\frac{Re_\infty}{Ma_\infty} \tag{14}$$

Spatial Discretization

For the solution, a finite-volume technique is applied. The flow equations have an integral form

$$\frac{d}{dt}\int_V U dV + \int_S \vec{F}(U)\cdot d\vec{S} = \int_V Q dV \tag{15}$$

for an arbitrary fixed region V with a boundary S. Performing the integrations for a computational cell i yields

$$V_i\frac{dU_i}{dt} = \sum_{faces} -S\hat{F} + V_i Q_i \tag{16}$$

where the sum is taken over the faces of the computational cell. The flux for the face is defined as

$$\hat{F} = n_x F + n_y G + n_z H \tag{17}$$

Here F, G and H are the fluxes defined by Eqs. (2–4) in the x-, y- and z-directions, respectively.

In the evaluation of the inviscid fluxes, Roe's method[7] is applied. The flux is calculated as

$$\hat{F} = T^{-1}F(TU) \tag{18}$$

where T is a rotation matrix which transforms the dependent variables to a local coordinate system normal to the cell surface. In this way only the Cartesian form F of the flux is needed. This is calculated from

$$F = \frac{1}{2}[F(U^l)+F(U^r)] - \frac{1}{2}\sum_{k=1}^{K} r^{(k)}|\lambda^{(k)}|\alpha^{(k)} \tag{19}$$

where U^l and U^r are the solution vectors evaluated on the left and right sides of the cell surface, $r^{(k)}$ is a Jacobian matrix $A = \partial F/\partial U = R\Lambda R^{-1}$, the corresponding eigenvalue is $\lambda^{(k)}$, and $\alpha^{(k)}$ is the corresponding characteristic variable obtained from $R^{-1}\Delta U$, where $\Delta U = U^r - U^l$. A MUSCL-type approach has been adopted for the evaluation of U^l and U^r. In the evaluation of U^l and U^r, primary flow variables (ρ, u, v, w, p), and conservative turbulent variables (ρk, $\rho\epsilon$) are utilized.

The characteristic variables which include the coupling with the kinetic energy of turbulence are

$$\begin{aligned}
\alpha^{(1)} &= (1-\frac{2}{3}\frac{k}{c^2})\delta\rho - \frac{1}{c^2}\delta p - \frac{2}{3}\frac{\rho}{c^2}\delta k \\
\alpha^{(2)} &= \frac{1}{2c^2}(\frac{2}{3}k\delta\rho + \rho c\delta u + \delta p + \frac{2}{3}\rho\delta k) \\
\alpha^{(3)} &= \rho\delta v \\
\alpha^{(4)} &= \rho\delta w \\
\alpha^{(5)} &= \frac{1}{2c^2}(\frac{2}{3}k\delta\rho - \rho c\delta u + \delta p + \frac{2}{3}\rho\delta k) \\
\alpha^{(6)} &= \rho\delta k \\
\alpha^{(7)} &= \rho\delta\epsilon
\end{aligned} \tag{20}$$

Calculation of the Viscous Fluxes and the Source Term

The viscous fluxes as well as the derivatives in Eq.(12) are evaluated using a thin-layer approximation. For example, in the calculation of P the velocity derivatives are approximated in the i-direction as

$$\begin{aligned}
(\frac{\partial u}{\partial x})_i &= \frac{(Sn_x u)_{i+1/2} - (Sn_x u)_{i-1/2}}{V_i} \\
&\approx \frac{(n_x u)_{i+1/2} - (n_x u)_{i-1/2}}{d_i}
\end{aligned} \tag{21}$$

where d_i is the cell thickness in the i-direction. Velocities at the cell surfaces are obtained as averages from the nodal values. In the computer code the thin-layer model can be activated in any coordinate direction. For the derivatives in the viscous fluxes on the surface $i+1/2$, Eq.(21) is applied for a shifted contol volume $V_{i+1/2}$.

The source term and the possible wall correction in the the turbulent viscosity are calculated similarly in the i-, j- and k-directions. As a result the source term may contain several wall terms, and the wall correction of turbulent viscosity is different in different coordinate directions if walls are present.

Boundary conditions

At the free-stream boundary the values of the dependent variables are kept as constants. In the flowfield, k and ϵ are limited to their free-stream values. In the calculation of the inviscid fluxes at the solid boundary, flux-difference splitting is not used. Since the convective speed is equal to zero on the solid surfaces, the only contribution to the inviscid surface fluxes arises from the pressure terms in the momentum equations. A second-order extrapolation is applied for the evaluation of the wall pressure.

The viscous fluxes on the solid surfaces are obtained by setting $u = v = w = 0$ on the wall. The central expression of the viscous terms is replaced by a second-order one-sided formula. The wall temperature is set to the free-stream stagnation temperature. The viscous fluxes of k and ϵ are also set to zero at the wall.

Solution Algorithm

The discretized equations are integrated in time by applying the *DDADI*-factorization [10]. This is based on the approximate factorization and on the splitting of the Jacobians of the flux terms. The resulting implicit stage consists of a backward and forward sweep in every coordinate direction. The sweeps are based on a first-order upwind differencing. In addition, the linearization of the source term is factored out of the spatial sweeps. The boundary conditions are treated explicitly, and a spatially varying time step is utilized.

The implicit stage can be written as follows

$$\begin{aligned}&[I+\frac{\Delta t}{V_i}(\partial_i^- S_{i+1/2}A_i^+ - \partial_i^+ S_{i-1/2}A_i^-)]\times\\&[I+\frac{\Delta t}{V_j}(\partial_j^- S_{j+1/2}B_j^+ - \partial_j^+ S_{j-1/2}B_j^-)]\times\\&[I+\frac{\Delta t}{V_k}(\partial_k^- S_{k+1/2}C_k^+ - \partial_i^+ S_{k-1/2}C_k^-)]\times\\&\qquad [I-\Delta t D_i]\Delta U_i = \frac{\Delta t}{V_i}\mathcal{R}_i\end{aligned} \tag{22}$$

where $\partial^-_{i,j,k}$ and $\partial^+_{i,j,k}$ are first-order spatial difference operators in the i, j and k directions, A, B and C are the corresponding Jacobian matrices, $D = \partial Q/\partial U$, and $\mathcal{R}_i$ is the right-hand side of Eq.(16). The Jacobians are calculated as

$$A^{\pm} = R(\Lambda^{\pm} + kI)R^{-1} \tag{23}$$

where $\Lambda^{\pm}$ are diagonal matrices containing the positive and negative eigenvalues, and k is a factor to ensure the stability of the viscous term. The idea of the diagonally dominant factorization is to put as much weight on the diagonal as possible. The tridiagonal equation sets resulting from Eq.(22) are replaced by two bidiagonal sweeps and a matrix multiplication in each direction.

The matrix inversion resulting from the source term linearization is performed before the axial sweeps. Several forms have been suggested for D. In order to improve stability, only negative source terms can be linearized. The terms related to the walls are not linearized here. Thus the only contribution arises from the dissipation terms of Eq.(11). Following Vandromme[11], the dissipation can be written in the k-equation as

$$-\rho\epsilon = -\frac{Re_\infty}{Ma_\infty}\frac{c_\mu}{\mu_T}(\rho k)^2 \tag{24}$$

Since the production term is positive, its linearization is not possible. However, there is a strong coupling between the flowfield, turbulent viscosity and the production term P. The stiffness of the equation set can be reduced by using the following trick

$$\frac{\partial P}{\partial U} = -\frac{P}{|\Delta U_{max}|} \tag{25}$$

In this way the maximum change of U caused by P is limited to $|\Delta U_{max}|$. The resulting Jacobian of the source term can be written as

$$\frac{\partial Q}{\partial U} = \begin{pmatrix} \frac{|P|}{|\Delta(\rho k)_{max}|} - 2\frac{\rho\epsilon}{\rho k} & 0 \\ 0 & \frac{|P|}{|\Delta(\rho\epsilon)_{max}|} - 2c_2\frac{\rho\epsilon}{\rho k} \end{pmatrix} \tag{26}$$

The maximum changes $|\Delta U_{max}|$ are evaluated using the current values of ρk and $\rho\epsilon$ as

$$|\Delta(\rho k)_{max}| = \rho k/C_k \qquad |\Delta(\rho\epsilon)_{max}| = \rho\epsilon/C_\epsilon \tag{27}$$

Since the turbulent viscosity is twice as sensitive to changes of k as to changes of ϵ, C_ϵ was set to 5, and $C_k = 2C_\epsilon$ in the present study.

There is a fundamental difficulty in the simulation of external flows, where large regions of essentially laminar flow are connected with turbulent regions near the flying vehicle and the wake. The values of the turbulence quantities may vary by orders of magnitude within a short distance. Occasionally, a tiny change Δk may be much larger than the current value of k, and it is possible that an unphysically large value of μ_T would result if ϵ does not increase correspondingly. Because of this, some further limitation either in μ_T or the turbulence quantities is necessary. After the implicit sweeps $\Delta\rho k$ is limited to 1/6 and $\Delta\rho\epsilon$ to 1/3 of their current values. Also the maximum size of μ_T is limited in order to guarantee physically reasonable values during the iteration. In the present test cases the specified upper limit of μ_T was so high that the steady state results are not affected by the limitation.

In order to accelerate the convergence, a multigrid cycling is used. The method of Jameson [12] with a V-cycle has been adopted. The basic implementation of the mulgrid cycling is described in [8] and is not changed because of the implementation of the $k-\epsilon$ model.

Since μ_T is a nonlinear function of the turbulence quantities and the shape of the boundary layer, the resulting turbulent viscosities on the coarser grid level may differ considerably from those evaluated on the fine grid level. In order to circumvent this, the turbulent viscosities were only calculated on the finest grid level and those values were transferred to the coarser grids. This procedure improves the robustness of the multigrid cycle significantly.

Wing Geometry And Computational Grid

The wing selected for these calculations is the round leading edge cropped delta wing used in the International Vortex Flow Experiment on Euler Code Validation[5]. The leading edge sweep angle is 65° and the wing has a taper ratio of 0.15. The reference length for the Reynolds number and moment coefficient is the root chord c_r. The wing profile is constant over the span and is defined at the root by

$$y = \begin{cases} \pm(0.1183\sqrt{x} - 0.2101x + 0.3501x^2 - 0.3406x^3) & 0 \le x \le 0.4 \\ \text{NACA 64A005} & 0.4 < x \le 1 \end{cases}$$

The grid we used in the calculations is a single-block structured 128 × 48 × 64 O–O grid. The wing surface is shown in Fig. 1. Since only symmetric cases are calculated, only half of the wing is modelled.

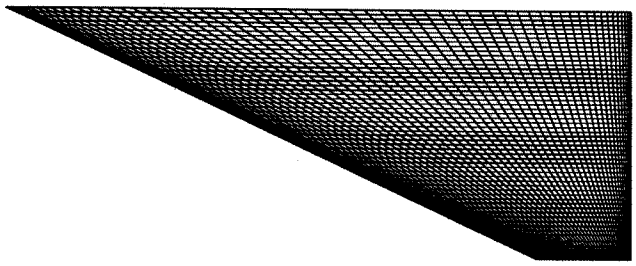

Fig.1. The grid on the surface of the cropped delta wing.

The outer edge of the grid with free-stream boundary conditions is a sphere centred at the middle of the root chord with a radius of $10c_r$. The reference point for the pitching moment calculation is $x = 0.57c_r$ and the reference length for the moment calculation is the root chord c_r. The grid is heavily clustered on the wing surface to obtain approximately 25 cells in the boundary layer. Previous experience suggests that this gives sufficient resolution inside the boundary layer. The height of the cells on the surface is about $3 \cdot 10^{-5}$, resulting in a y^+ value of the order of 1 in the middle of the first cell. The grid is also slightly clustered on the leading edge and the trailing edge and also on the tip to obtain better resolution in areas of large gradients. The grid is nearly orthogonal on the wing surface except at the trailing edge and the tip. The volume grid is generated using a transfinite interpolation method.

Results

Test Case $Re_\infty = 4.5 \times 10^6$ and $\alpha = 10.76°$
This flow case has previously been calculated by Kaurinkoski & Siikonen[6] assuming laminar flow and assuming turbulent flow with the Cebeci–Smith turbulence model. In the present study, a comparison is made with the previous results.

Transition of the boundary layer was not modelled separately; instead, the turbulence model was allowed to predict the location of transition. In this case the free-stream values of the turbulence quantities were set to $k = 4 \times 10^{-8}$ and $\epsilon = 1 \times 10^{-8}$. The effect of the free-stream values on the solution was not studied. The initial conditions were $k = 0.000038$ and $\mu_T = 1$. The value of k corresponds to a turbulence intensity of 0.005.

The aerodynamic force coefficients obtained for this case are shown in Table 1. As a comparison, the results with a laminar boundary layer and the Cebeci–Smith model are also shown. The experimental results are from Ref.[13]. It is seen that the $k-\epsilon$ results for C_L and C_D are only marginally improved from the results with the Cebeci–Smith model, whereas the predicted pitching moment coefficient $C_{m,57}$ is worse with the $k-\epsilon$ model.

The pressure coefficient distributions at cross-sections $x/c_r = 0.3$, $x/c_r = 0.6$ and $x/c_r = 0.8$ are shown on the left hand side of Fig. 2. It can be seen that the $k-\epsilon$ model produces results clearly different from the previous calculations. Most of the gradients in the spanwise direction are smeared out. As a result, the suction peak is somewhat underestimated, especially at $x/c_r = 0.8$. This is partly a result of the very high turbulent viscosities produced by the $k-\epsilon$ model. Although not shown here, 3D-visualizations of the results show that the vortex core is highly turbulent. In light of the errors in the pressure distributions, the turbulence of the vortex core seems doubtful.

Table 1. The lift, drag and pitching moment coefficients at $\alpha = 10.76°$, $Ma = 0.85$ and $Re = 4.5 \cdot 10^6$ with various boundary layer types.

$\alpha = 10.76°$, $Re = 4.5 \cdot 10^6$, $Ma = 0.85$			
	C_L	C_D	$C_{m.57}$
$k-\epsilon$	0.4908	0.0869	-0.0121
Laminar[6]	0.5057	0.0862	-0.0140
Cebeci–Smith[6]	0.4935	0.0867	-0.0118
Experiments[13]	0.4632	0.0906	-0.0086

The surface streamlines and the corresponding pressure coefficient distributions on the upper surface for this case are plotted in Figs. 3 and 4, and for the case $\alpha = 19.48°$ in Figs. 5 and 6. Compared with the results from Ref.[6], the vortex is seen to be wider than that obtained using the Cebeci–Smith model. Also, only one vortex is formed, whereas the results from Ref.[6] showed also a clear secondary separation line with the associated secondary vortex.

The total pressure contours at cross-sections $x/c_r = 0.3$, $x/c_r = 0.6$, $x/c_r = 0.8$ and $x/c_r = 1.05$ are seen in Fig. 7. Again, the results with the Cebeci–Smith model are shown for comparison. These plots confirm the conclusions concerning the width of the primary vortex and the secondary vortex.

Fig. 8 shows the velocity profiles at four stations. The inflection point at $i = 76$ is due to the primary vortex. The turbulent viscosity distributions in Fig. 9 are seen to form a set of almost similar curves, except for the curve $i = 68$. Fig. 10 shows the k distribution, and here also, a distinct peak at $i = 76$ is seen to develop due to the primary vortex.

The convergence history of the aerodynamic coefficients is plotted in Fig. 11. The convergence of the lift coefficient C_L is typical for the $k-\epsilon$ model: a very restless development is seen and the same property is also seen from the C_D and C_m curves. The efficiency of the multigrid method is demonstrated in Fig. 12: The convergence history of the L_2-norm of the density residual is plotted with one grid level and three grid levels. In the former case 5 000 cycles were required for convergence, whereas in the latter case sufficient convergence was obtained within 500 cycles.

Test Case $Re_\infty = 4.5 \times 10^6$ and $\alpha = 19.48°$
The pressure coefficient distributions at cross-sections $x/c_r = 0.3$, $x/c_r = 0.6$ and $x/c_r = 0.8$ are shown on the right hand side of Fig. 2. Again, the vortex width is seen to be larger than with the Cebeci–Smith model. At $x/c_r = 0.3$ the rapid suction rise at the edge of the vortex is not properly captured and the suction peak is underestimated. At $x/c_r = 0.6$ the details of the suction peak are smeared out as a result of high turbulent viscosities. At $x/c_r = 0.8$ the average suction level is rather good, but the distribution is not correct. The surface streamlines and the pressure coefficient distribution plotted in Figs. 5 and 6 indicate vortex bursting at $x/c_r \approx 0.8$, which is in agreement with the experimental result $x/c_r \approx 0.82$[5].

The aerodynamic force coefficients obtained for this case are shown in Table 2. For comparison, the results with the Cebeci–Smith model[6] and the experimental results[13] are also shown. The $k-\epsilon$ model predicts the integrated force coefficients C_L and C_D more accurately. The pitching moment, however, is in error. This indicates a false chordwise pressure distribution but good average pressure level. The error in the location of the aerodynamic center is, however, only $0.025c_r$.

Table 2 The lift, drag and pitching moment coefficients at $\alpha = 19.48°$, $Ma = 0.85$ and $Re = 4.5 \cdot 10^6$ with various boundary layer types.

$\alpha = 19.48°$, $Re = 4.5 \cdot 10^6$, $Ma = 0.85$			
	C_L	C_D	$C_{m.57}$
$k-\epsilon$	0.8398	0.2827	-0.0043
Cebeci–Smith[6]	0.8154	0.2765	-0.0120
Experiments[13]	0.8970	0.3082	-0.0269

Conclusions

Transonic viscous flow past a cropped delta wing has been calculated using a low-Reynolds number $k-\epsilon$ model. In comparison with the earlier results obtained using algebraic turbulence models, the quality of the result is slightly improved but the convergence speed of the new model is lower.

The $k-\epsilon$ model is seen to be highly sensitive to the initial and boundary values specified for the case. Despite this, more physical information is obtained from the flow field, since the turbulence model is not functionally bound to a solid wall but can produce turbulence from the gradients in the flow field.

The $k-\epsilon$ model turns out to be slightly better than the Cebeci–Smith model with respect to integrated forces. The turbulence intensity inside the vortex core is, however, suspiciously high and further improvements are needed for reliable simulations.

References

1. STOCK, H.W., HAASE, W., Determination of Length Scales in Algebraic Turbulence Models for Navier-Stokes Methods, AIAA Journal, Vol. 27, No. 1, Jan. 1989.

2. BALDWIN, B.S., LOMAX, H., Thin Layer Approximation and Algebraic Model for Separated Turbulent Flows, AIAA Paper 78-257, Jan., 1978.

3. LAUNDER, B.E., SPALDING, B., Mathematical Models of Turbulence, Academic Press, New York, 1972.

4. CHIEN, K., Predictions of Channel and Boundary-Layer Flows with a Low-Reynods-Number Turbulence Model, AIAA Journal, Vol.20, No.1, Jan. 1982, pp.33-38.

5. Proceedings of the Symposium on International Vortex Flow Experiment on Euler Code Validation, Edited by A. ELSENAAR and G. ERIKSSON, Stockholm, Sweden, Oct, 1986.

6. KAURINKOSKI, P., and SIIKONEN, T., Calculation of Transonic Laminar and Turbulent Flow Past a Delta Wing, Helsinki University of Technology, Laboratory of Aerodynamics, Report No. A-13, Series A, 1992, ISBN 951–22–1273–0.

7. ROE, P.L., Approximate Riemann Solvers, Parameter Vectors, and Difference Schemes, Journal of Computational Physics, Vol. 43, 1981.

8. SIIKONEN, T., HOFFREN, J. and LAINE, S., A Multigrid *LU* Factorization Scheme for the Thin-Layer Navier–Stokes Equations, 17th ICAS Congress, Stockholm, 1990.

9. SIIKONEN, T., An Application of Roe's Flux-Difference Splitting for the $k-\epsilon$ Turbulence Model, Helsinki University of Technology, Laboratory of Aerodynamics, Report No. A-15, Series A, 1994, ISBN 951–22–2059–8.

10. LOMBARD, C.K., BARDINA, J., VENKATAPATHY, E., Multi-Dimensional Formulation of CSCM — An Upwind Flux Difference Eigenvector Split Method for the Compressible Navier–Stokes Equations, 6th AIAA Computational Fluid Dynamics Conference, Danvers, Massachusetts, 1983.

11. VANDROMME, D., Turbulence Modeling for Turbulent Flows and Implementation in Navier-Stokes Solvers, in: Introduction to the Modeling of Turbulence, VKI Lecture Series 1991-02.

12. JAMESON, A., YOON, S., Multigrid Solution of the Euler Equations Using Implicit Schemes, AIAA Journal, Vol. 24, No.11, 1986.

13. HARTMANN, K., US/European Transonic Vortex Flow Experiment — Data Lists of Force Measurements, DFVLR, IB 222 – 86 A 03, Göttingen, 1986.

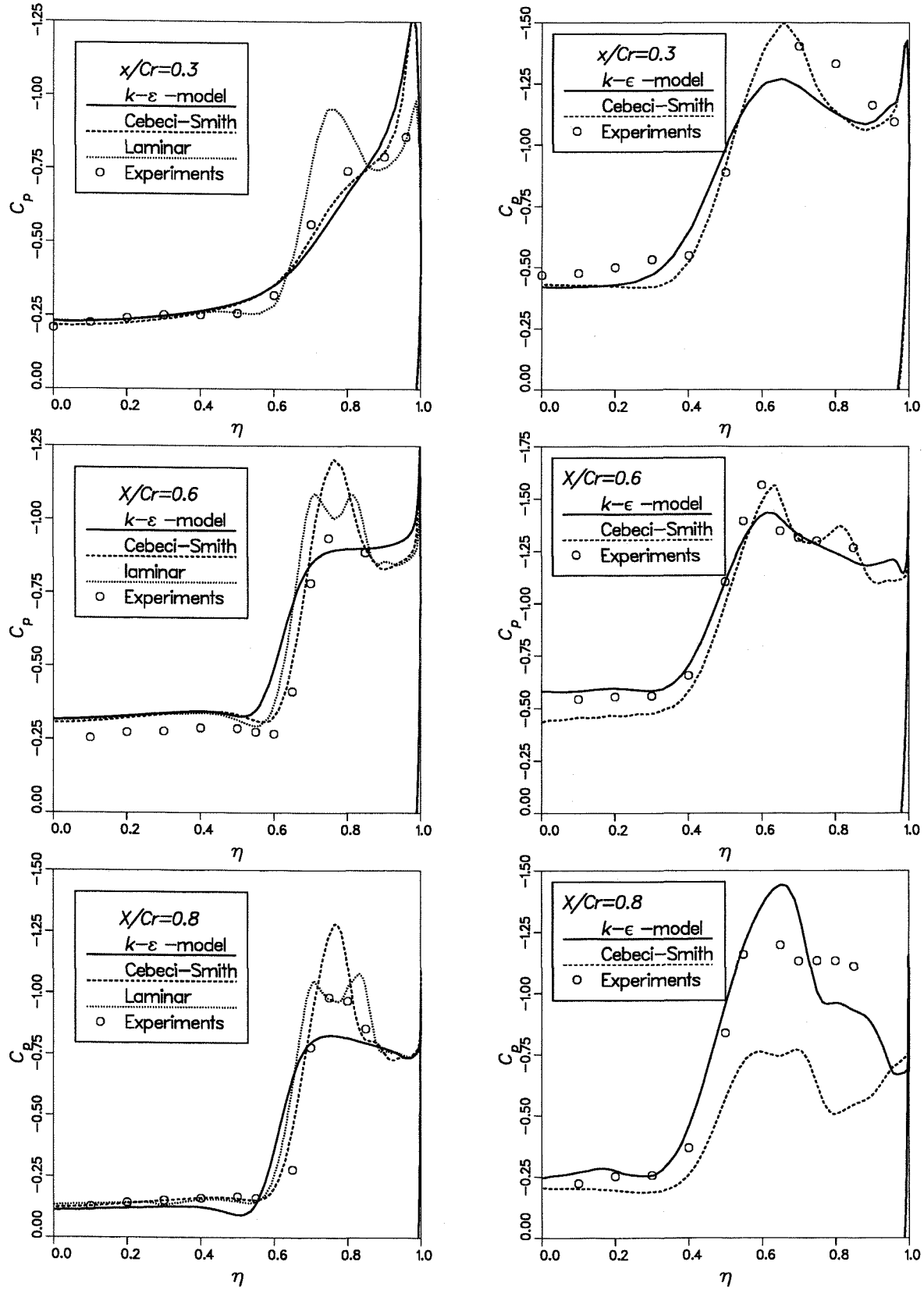

Fig.2. C_p-distributions at $x/c_r = 0.3$, 0.6 and 0.8 for $\alpha = 10.76°$ (left) and for $\alpha = 19.48°$ (right) as calculated with the $k - \epsilon$ model, the Cebeci–Smith model[6] and with a laminar flow assumption[6]. $Re_\infty = 4.5 \times 10^6$ and $Ma_\infty = 0.85$. The experimental results are from Ref.[5].

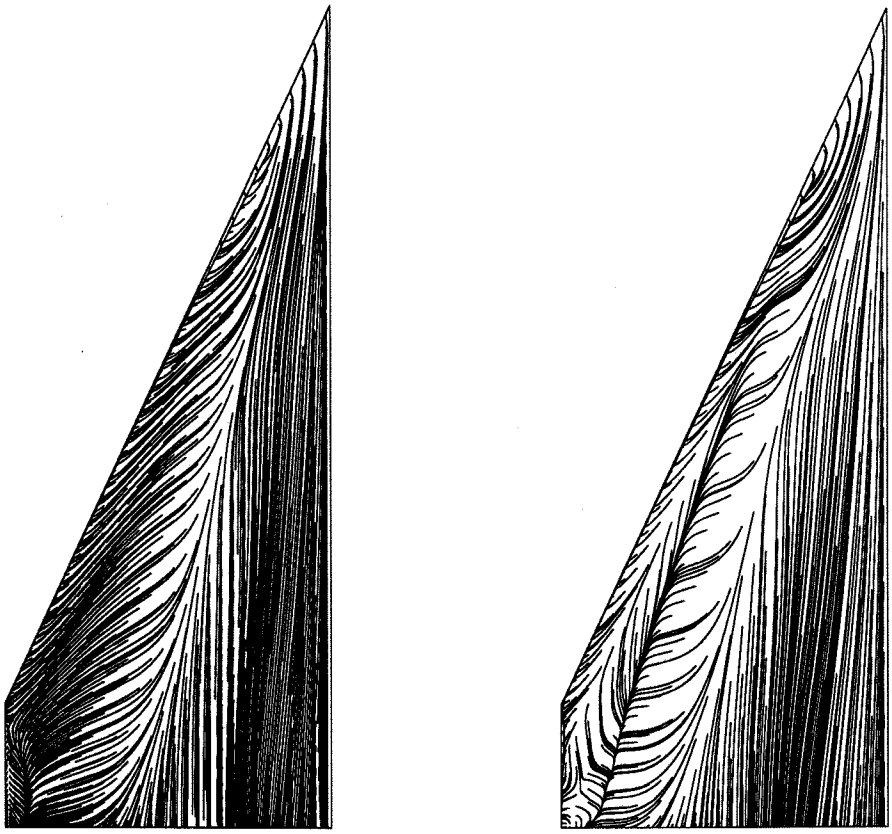

Fig.3. Surface streamlines of $\alpha = 10.76°$ using the $k - \epsilon$ model (left) and the Cebeci–Smith turbulence model[6] (right) at $Re_\infty = 4.5 \times 10^6$ and $Ma_\infty = 0.85$.

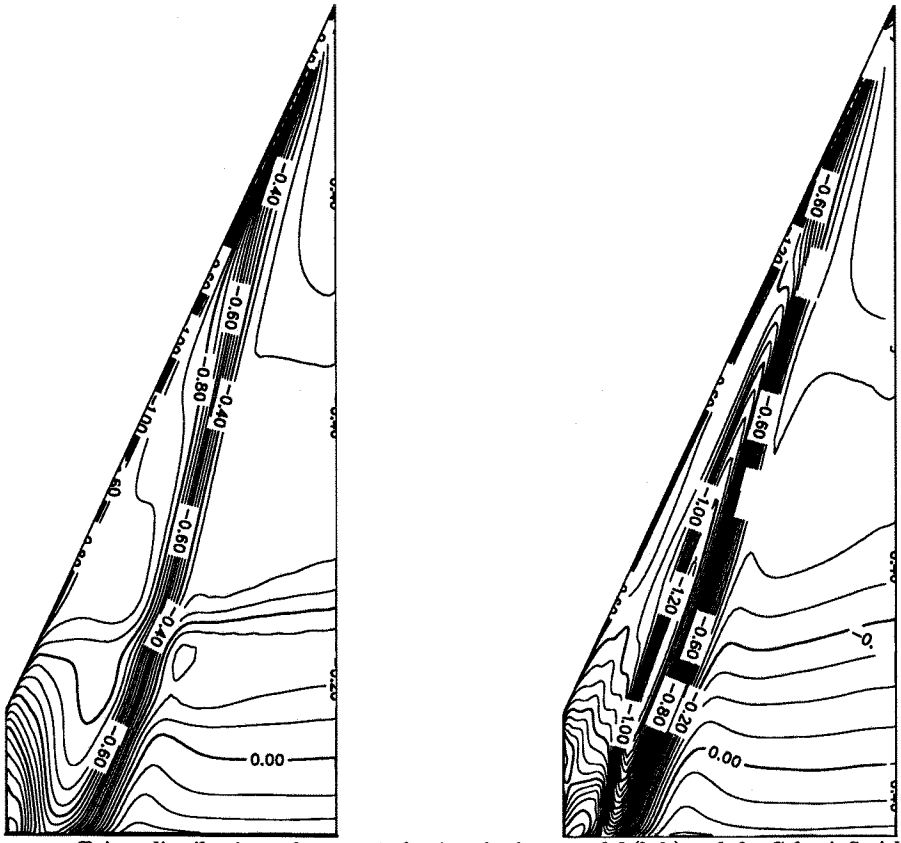

Fig.4. Pressure coefficient distributions of $\alpha = 10.76°$ using the $k-\epsilon$ model (left) and the Cebeci–Smith turbulence model[6] (right) at $Re_\infty = 4.5 \times 10^6$ and $Ma_\infty = 0.85$.

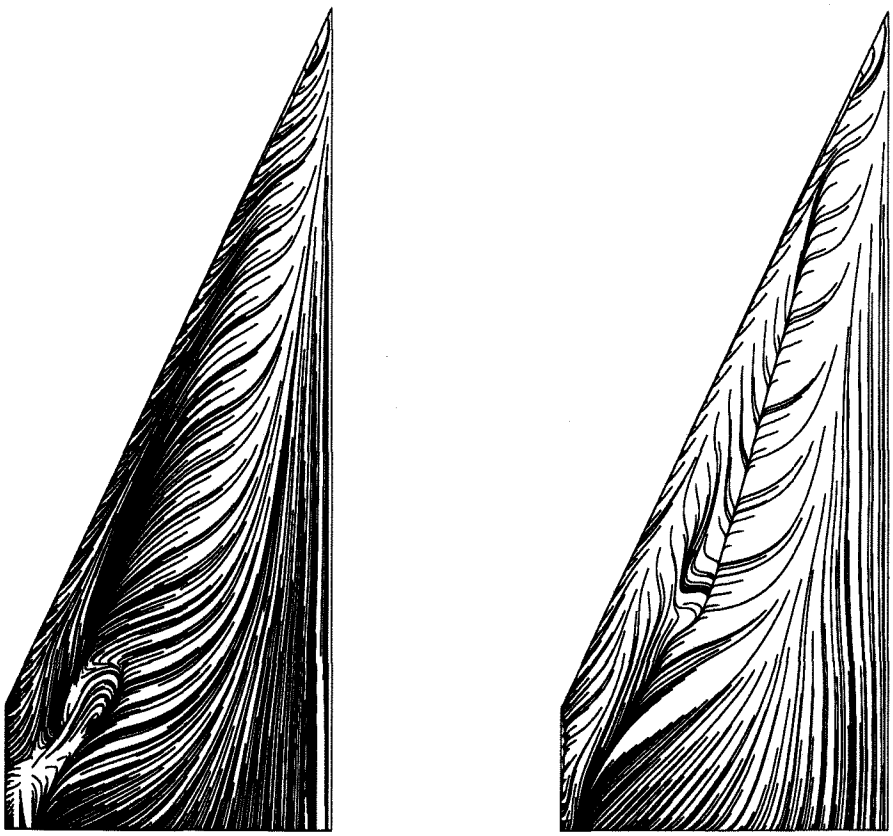

Fig.5. Surface streamlines of $\alpha = 19.48°$ using the $k - \epsilon$ model (left) and the Cebeci–Smith turbulence model[6] (right) at $Re_\infty = 4.5 \times 10^6$ and $Ma_\infty = 0.85$.

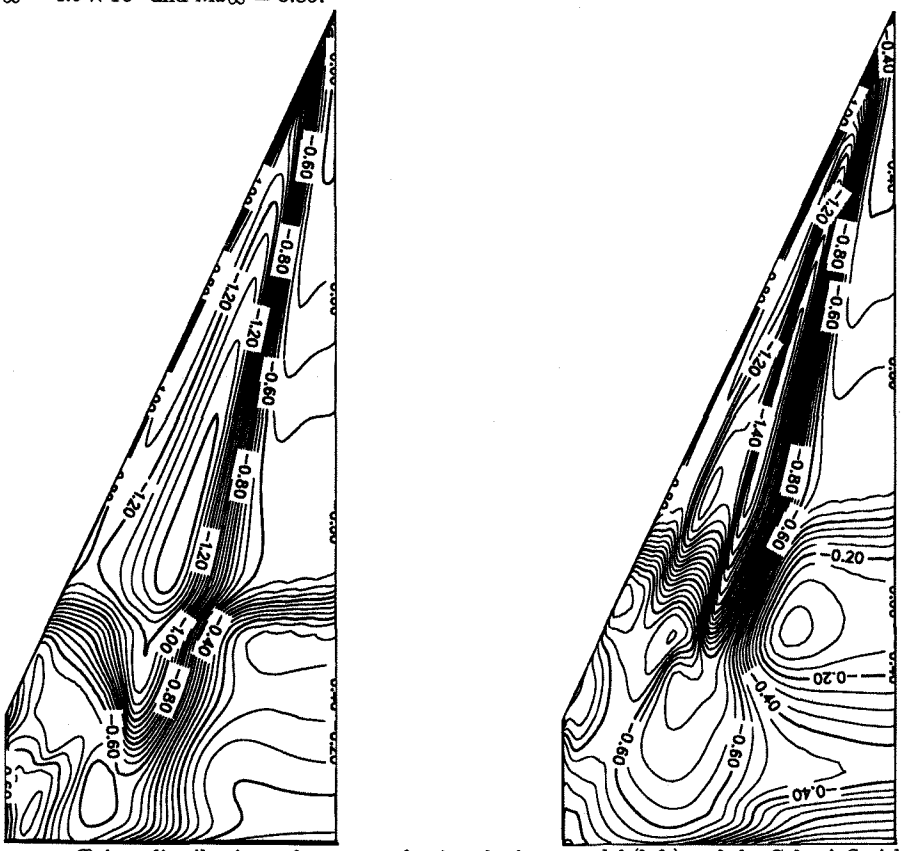

Fig.6. Pressure coefficient distributions of $\alpha = 19.48°$ using the $k - \epsilon$ model (left) and the Cebeci–Smith turbulence model[6] (right) at $Re_\infty = 4.5 \times 10^6$ and $Ma_\infty = 0.85$.

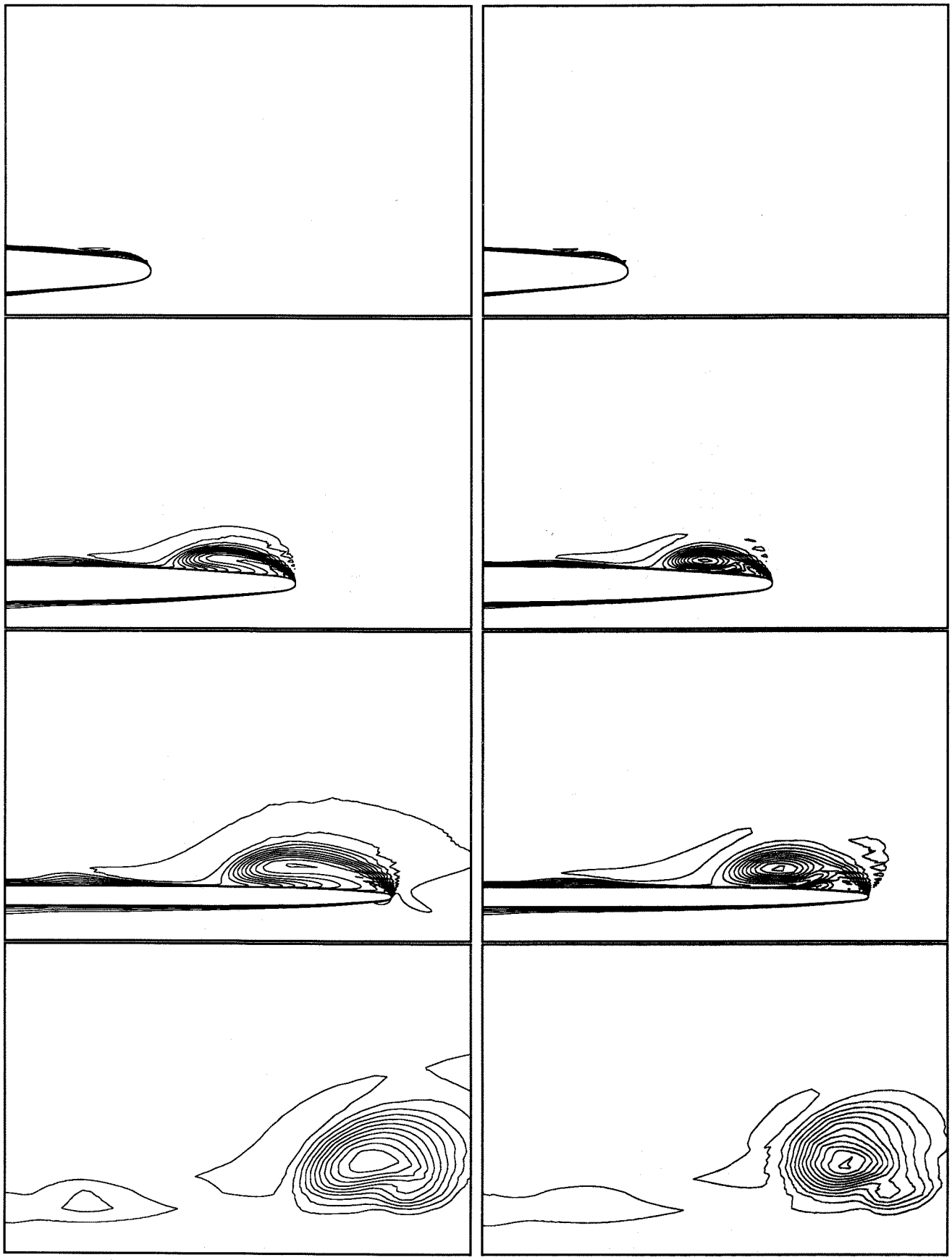

Fig.7. Total pressure distributions at $x/c_r = 0.3$, 0.6, 0.8 and 1.05 for $\alpha = 10.76°$ using the $k-\epsilon$ model (left) and the Cebeci–Smith model[6] (right) at $Re_\infty = 4.5 \times 10^6$ and $Ma_\infty = 0.85$. $\Delta p_0/\rho_\infty c_\infty^2 = 0.05$.

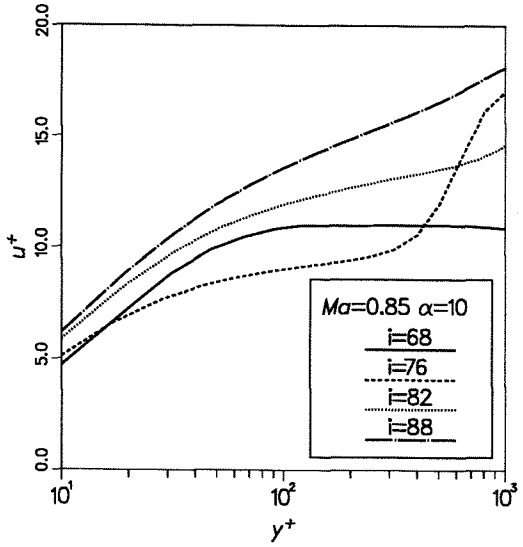

Fig. 8. Velocity profiles at $2y/b = 0.27$. $\alpha = 10.76°$ and $Re_\infty = 4.5 \times 10^6$. $x/c_r = 0.234$, 0.284, 0.356 and 0.450, respectively.

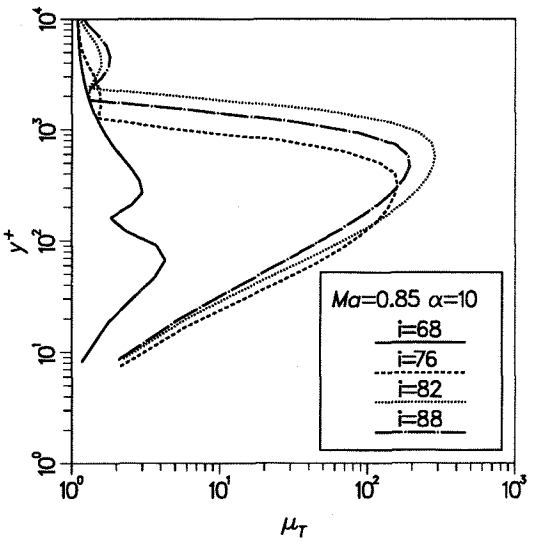

Fig. 9. Turbulent viscosity μ_T at $2y/b = 0.27$. $\alpha = 10.76°$ and $Re_\infty = 4.5 \times 10^6$. $x/c_r = 0.234$, 0.284, 0.356 and 0.450, respectively.

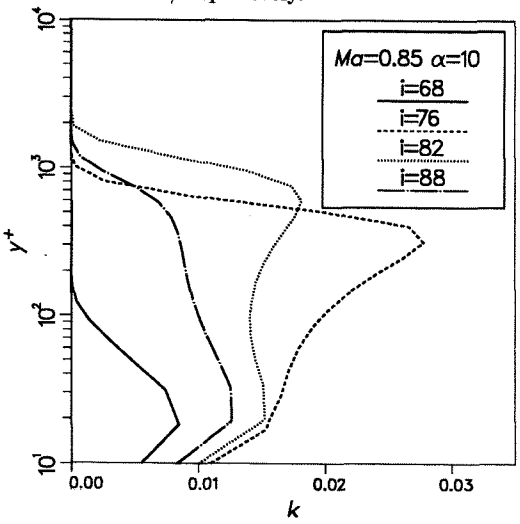

Fig. 10. Turbulence kinetic energy k at $2y/b = 0.27$. $\alpha = 10.76°$ and $Re_\infty = 4.5 \times 10^6$.

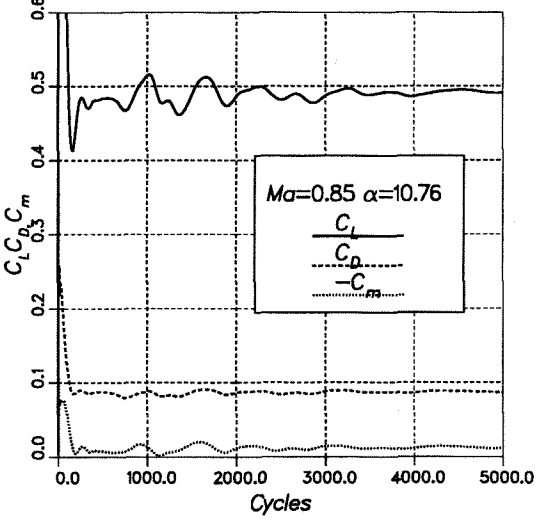

Fig. 11. Convergence of C_L, C_D and C_m at $\alpha = 10.76°$ and $Re_\infty = 4.5 \times 10^6$ with one multigrid level.

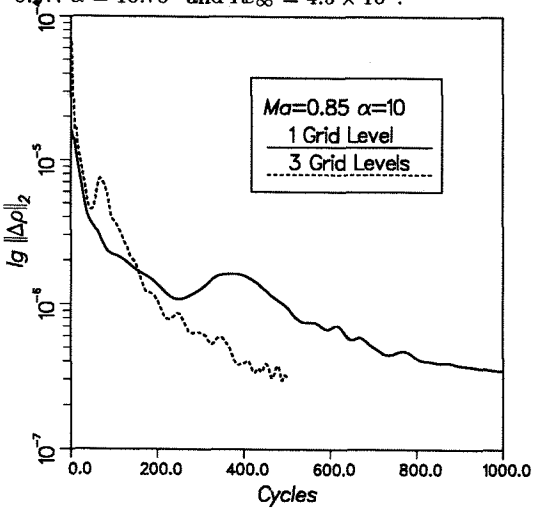

Fig. 12. The convergence history of $\lg ||\Delta\rho||_2/n$ using one grid level (solid line) and three grid levels (broken line).